Ultrasonics - Sonochemistry 40 (2018) 944–954

Contents lists available at ScienceDirect

Ultrasonics - Sonochemistry

journal homepage: www.elsevier.com/locate/ultson

Numerical study of acoustically driven bubble cloud dynamics near a rigid wall

Jingsen Ma, Chao-Tsung Hsiao*, Georges L. Chahine

Dynaflow, Inc., 10621-J Iron Bridge Road, Jessup, MD, USA

ARTICLE INFO

Keywords:
Bubble cloud
Cavitation
Bubble dynamics
Erosion
Cleaning

ABSTRACT

The dynamics of a bubble cloud excited by a sinusoidal pressure field near a rigid wall is studied using a novel Eulerian/Lagrangian two-phase flow model. The effects of key parameters such as the amplitude and frequency of the excitation pressure, the cloud and bubble sizes, the void fraction, and the initial standoff distance on the bubbles' collective behavior and the resulting pressure loads on the nearby wall are investigated. The study shows that nonlinear bubble cloud dynamics becomes more pronounced and results in higher pressure loading at the wall as the excitation pressure amplitude increases. The strongest collective bubble behavior occurs at a preferred resonance frequency. At this resonance frequency, pressure peaks orders of magnitudes higher than the excitation pressure result from the bubble interaction when the amplitude of the pressure excitation is high. The numerically obtained resonance frequency is significantly different from the reported natural frequency of a spherical cloud derived from linear theory, which assumes small amplitude oscillations in an unbounded medium. At high amplitudes of the excitation, the resonance frequency decreases almost linearly with the ratio of excitation pressure amplitude to ambient pressure until the ratio is larger than one.

1. Introduction

Cloud cavitation is known to be one of the most damaging types of cavitation due to the generated high pressure loading [1–10] on nearby structures during collective bubble collapse. It occurs in various engineering applications such as in Shock Wave Lithotripsy (SWL) for kidney stone fragmentation [11–13], cavitating jets for cutting, cleaning [14–16], oxidation [17], disinfection [18], or biomass processing [19], cavitation on propellers [20], cavitation erosion testing [21] etc.

Numerical modeling of bubble cloud dynamics near a rigid wall is challenging because it involves bubble-bubble, bubble-flow, and bubble-wall interactions. In addition, the problem involves multi-scale physics ranging from micron-scale individual bubbles to meter-scale flow field. Many numerical studies have been dedicated to modeling the cloud bubbles dynamics. Among them are asymptotic expansions methods [5,22], Boundary Element Method (BEM) simulations [7], and Direct Numerical Simulation (DNS) [23,24]. However, due to the computational cost, these methods are mostly limited to small scale problems addressed for fundamental study purposes, such as developing subgrid relationships for larger scale models. For practical applications, two-phase bubbly flows are usually modeled using one of several approaches: equivalent homogeneous continuum models, Eulerian two-fluid models, or Eulerian-Lagrangian approaches [25] wherein the bubbles are treated as discrete particles. Homogeneous models are useful for low void fractions, whereas Eulerian-Lagrangian approaches are more appropriate for higher void fractions [26,27].

In one of our previous studies an Eulerian-Lagrangian two-phase flow model was compared with different numerical models [28]. These models were assessed for the simulation of a cloud of bubbles interacting with a large exploding bubble in a viscous liquid. It was found that, although all the models capture similarly the average low-frequency dynamics, the microscale response of the discrete bubbles and the resultant high-frequency local fluctuations are properly captured by the Eulerian-Lagrangian solver only. This highlights that a discrete bubble modeling approach is essential to a better description of such problems since it can resolve the physics down to the single bubble scale, while maintaining computational cost affordability and properly capturing the overall large-scale flow behavior.

The Eulerian-Lagrangian two-phase flow model we consider here treats the two-phase mixture as a continuum and solves the Navier-Stokes equations using Eulerian grids with a time and space varying density [8,29]. The microbubbles are modeled as interacting singularities representing moving and oscillating spherical bubbles, which are described by modified Rayleigh-Plesset-Keller-Herring equations and are tracked in a Lagrangian fashion. Higher order bubble deformations

* Corresponding author.
E-mail address: ctsung@dynaflow-inc.com (C.-T. Hsiao).

http://dx.doi.org/10.1016/j.ultsonch.2017.08.033
Received 23 November 2016; Received in revised form 26 July 2017; Accepted 28 August 2017
Available online 31 August 2017
1350-4177/

can also be included but are not considered here. A two-way coupling between the two-phase medium and the discrete bubbles is realized through the local mixture density deduced from the bubble sizes and distribution and their time and space variations.

In this paper we apply the method to investigate the physics involved in collective bubble cloud dynamics and compute the pressures on a nearby flat rigid wall for a bubble cloud excited by an imposed sinusoidal pressure field [8]. Parametric studies are conducted on key parameters such as the amplitude and frequency of the excitation pressure, the initial cloud and bubble sizes, and the initial cloud void fraction.

2. Numerical model

The two-phase flow model employed in this study has been extensively validated and documented in previous studies. These included investigations of the effects of a propeller flow on bubble size distribution in water [30,31], modeling of propeller tip vortex cavitation inception [31,32], simulation of bubbly flows in a bubble augmented propulsor [33], bubble entrainment in plunging jets [34] and wave propagation in bubbly media [8,28,29,35], etc. In this two-phase flow approach an Eulerian scheme is used to solve the continuum-based two-phase medium and is coupled with a discrete bubble model tracking bubble motion in a Lagrangian fashion. The two-way coupling between the Eulerian continuum-based model and the Lagrangian discrete bubble model is realized as follows:

- The dynamics and motion of the individual bubbles in the flow field are controlled by the two-phase medium local properties and gradients.
- The local properties of the mixture (void fractions and local densities) are determined by the instantaneous bubble sizes and distribution.
- The mixture flow field has an evolving density distribution, which is space and time dependent, and satisfies mass and momentum conservation.

2.1. Eulerian continuum-based two-phase model

The two-phase medium continuum model uses a viscous flow code 3DynaFS-Vis©, which solves the Navier-Stokes equations and satisfies the continuity and momentum equations:

$$\frac{\partial \rho_m}{\partial t} + \nabla\cdot(\rho_m \mathbf{u}) = 0, \tag{1}$$

$$\rho_m \frac{D\mathbf{u}}{Dt} = -\nabla p + \mu_m \nabla^2 \mathbf{u}, \tag{2}$$

where the subscript m represents the mixture properties. $\mathbf{u}$ is the local mixture velocity, p is the local pressure. The mixture density, ρ_m, and the mixture viscosity, μ_m, can be expressed as functions of the gas volume fraction α:

$$\rho_m = (1-\alpha)\rho_l + \alpha\rho_g, \quad \mu_m = (1-\alpha)\mu_l + \alpha\mu_g, \tag{3}$$

where the subscript l represents the liquid and the subscript g represents the gas. The equivalent medium has a time and space dependent density since the void fraction α varies in both space and time. This makes the overall flow field problem similar to a compressible flow problem. In our approach, which couples the continuum medium with the discrete bubbles, the mixture density is not an explicit function of the pressure through an equation of state. Instead, tracking the bubbles and knowing their concentration provides α and ρ_m as functions of space and time.

The system of equations is solved by an artificial compressibility method [36] in which a pseudo-time derivative of the pressure multiplied by an artificial-compressibility factor, β, is added to the continuity equation as

$$\frac{1}{\beta}\frac{\partial p}{\partial \tau} + \frac{\partial \rho_m}{\partial t} + \nabla\cdot(\rho_m \mathbf{u}) = 0. \tag{4}$$

As a consequence, a hyperbolic system of equations is formed and can be solved using a time marching scheme. The solutions are iterated in the pseudo-time until convergence. β is selected to obtain converged solutions with a good convergence speed. Following our previous studies [8], we have selected $\beta = 100$ for all the simulation cases. To obtain a time-dependent solution, a Newton iterative procedure is performed at each physical time step in order to satisfy the continuity equation.

3DynaFS-Vis© uses a finite volume formulation. First-order Euler implicit differencing is applied to the time derivatives. The spatial differencing of the convective terms uses the flux-difference splitting scheme based on Roe's method [37] and van Leer's MUSCL method [38] for obtaining the first-order and the third-order fluxes, respectively. A second-order central differencing is used for the viscous terms which are simplified using the thin-layer approximation. The flux Jacobians required in an implicit scheme are obtained numerically. The resulting system of algebraic equations is solved using the Discretized Newton Relaxation method [39] in which symmetric block Gauss-Seidel sub-iterations are performed before the solution is updated at each Newton iteration.

2.2. Lagrangian discrete bubble model

The Lagrangian discrete bubble model, 3DynaFS-Dsm©, uses a discrete singularity model where averaging over the bubble surface is applied to the local fluid quantities [40] This model has been shown to produce accurate results when compared to full 3D two-way interaction computations [41] The averaging scheme allows one to consider only a spherical equivalent bubble and use a modified Rayleigh-Plesset-Keller-Herring equation [42,43] to describe the bubble dynamics,

$$\left(1-\frac{\dot R}{c_m}\right)R\ddot R + \frac{3}{2}\left(1-\frac{\dot R}{3c_m}\right)\dot R^2 = \frac{\mathbf{u}_s^2}{4} + \frac{1}{\rho_m}\left(1+\frac{\dot R}{c_m}+\frac{R}{c_m}\frac{d}{dt}\right)\left[p_v + p_{g0}\left(\frac{R_0}{R}\right)^{3k} - p_{enc} - \frac{2\gamma}{R} - 4\mu_m\frac{\dot R}{R}\right], \tag{5}$$

where c_m is the local sound speed in the mixture [44], which is related to the local void fraction, α, by

$$c_m^2 = \frac{p}{\rho_l}\frac{\left[1+\frac{\alpha}{1-\alpha}\right]^2}{\left[\frac{1}{k}\frac{\alpha}{1+\alpha} + \frac{p}{\rho_l c_l^2}\right]}, \tag{6}$$

where c_l the sound speed in the pure liquid. The slip velocity, $\mathbf{u}_s = \mathbf{u}_{enc} - \mathbf{u}_b$, is the difference between the bubble encountered liquid velocity, $\mathbf{u}_{enc}$, and the bubble translation velocity, $\mathbf{u}_b$. R and R_0 are the bubble radii at times t and 0. p_v is the liquid vapor pressure, P_{g0} is the initial bubble gas pressure, k is the polytropic compression constant, and $\mathbf{u}_{enc}$ and p_{enc} are respectively the averages of the liquid velocities and pressures over the bubble surface if the bubble was not present.The bubble trajectory is obtained from the following bubble motion equation:

$$\frac{d\mathbf{u}_b}{dt} = \left(\frac{\rho_l}{\rho_g}\right)\left[\frac{3}{8R}C_D|\mathbf{u}_s|\mathbf{u}_s + \frac{1}{2}\left(\frac{d\mathbf{u}_{enc}}{dt} - \frac{d\mathbf{u}_b}{dt}\right) - \frac{\nabla p}{\rho_l} + \frac{(\rho_b-\rho_l)}{\rho_l}g + \frac{3C_L}{4\pi}\frac{\sqrt{\nu}}{R}\frac{\mathbf{u}_s\times\boldsymbol{\Omega}}{\sqrt{|\boldsymbol{\Omega}|}} + \frac{3\dot R}{2R}\mathbf{u}_s\right], \tag{7}$$

where C_D is the bubble drag coefficient given by an empirical equation from [45]. C_L is a lift coefficient equal to 6.44 and Ω is the vorticity vector. The first right hand side term is a drag force. The second term accounts for the added mass. The third term accounts for the presence of a pressure gradient, while the fifth term accounts for gravity and the sixth term is a lift force [46]. The last term is the Bjerknes force term

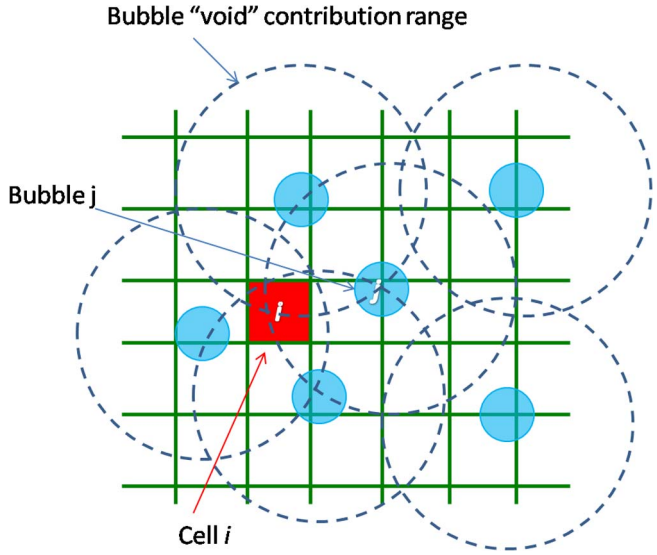

Fig. 1. Illustration of the void fraction computation scheme using a Gaussian distribution scheme.

due to coupling between bubble volume variations and bubble motion [47–49].

2.3. Void fraction computation

A key of the Eulerian-Lagrangian coupling is the computation of the void fraction from the instantaneous bubble sizes and locations. This is achieved by using a Gaussian distribution scheme, which smoothly "spreads" each bubble's volume over neighboring cells in a prescribed radial distance while conserving the total gas volume [35]. Fig. 1 illustrates the void fraction computation scheme for a representative cell *i*. In this scheme, the "void" contribution, $v_{i,j}$, of a bubble *j* to a nearby cell *i* can be expressed as:

$$v_{i,j} = V_j^b e^{-\frac{|\mathbf{x}_{i,j}|^2}{2(\lambda R_j)^2}}, \tag{8}$$

where V_j^b is the volume of bubble *j*, R_j is the radius of bubble *j*, λR_j is the standard deviation of the Gaussian distribution function, $\mathbf{X}_{i,j}$ is the position vector between bubble *j* and cell *i*. In order to guaranty that the total volume of the bubbles is conserved Eq. (8) is normalized using a cell-volume-weighted normalization scheme:

$$\bar{v}_{i,j} = \frac{v_{i,j} V_i^{cell}}{\sum_k^{N_{cells}} v_{k,j} V_k^{cell}} V_j^b, \tag{9}$$

where V_i^{cell} is the volume of cell *i*. Each bubble contribute its "void" effects to a limited number, N_{cell}, of nearby cells due to the Gaussian decay. To compute the void fraction for the cell *i* we then sum up the "void" contribution from all N_i bubbles, which are within the "influence range" and divide by the cell volume,

$$\alpha_i = \sum_{j=1}^{N_i} \frac{\bar{v}_{i,j}}{V_i^{cell}} = \sum_{j=1}^{N_i} \frac{v_{i,j} V_j^b}{\sum_k^{N_{cells}} v_{k,j} V_k^{cell}}. \tag{10}$$

The sensitivity of the results to the selected value of the standard deviation, λR_j, of the Gaussian distribution function is evaluated for different values of λ. Fig. 2 illustrates this influence by presenting, as a function of λ, the maximum pressure generated on the wall center for $P_0 = 10$ atm, $P_{amp} = 9$ atm, $R_0 = 50$ μm, $f = 12$ kHz, $\alpha_0 = 5\%$ and $A_0 = X_0 = 1.5$ mm. It is seen that as long as λ is less than 3 there is little dependency of the results on its value. In the results shown below $\lambda = 2.75$ is used.

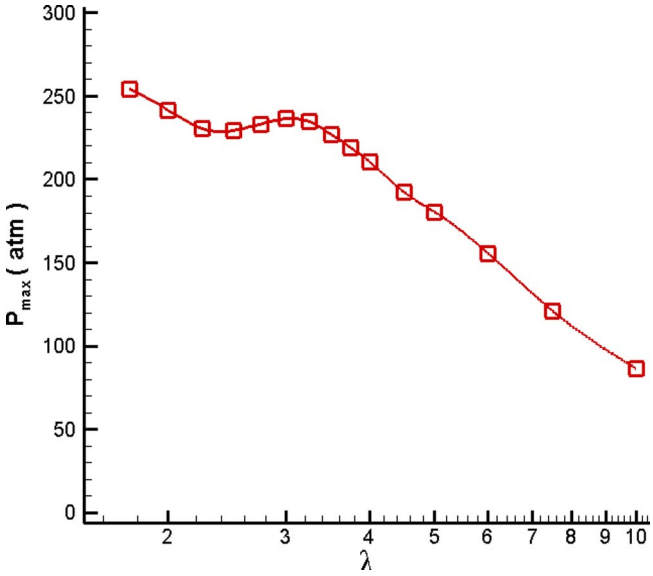

Fig. 2. Illustration of the effect of λ on the maximum pressure at the wall center. $P_0 = 10$ atm, $P_{amp} = 9$ atm, $R_0 = 50$ μm, $f = 12$ kHz, $\alpha_0 = 5\%$ and $A_0 = X_0 = 1.5$ mm.

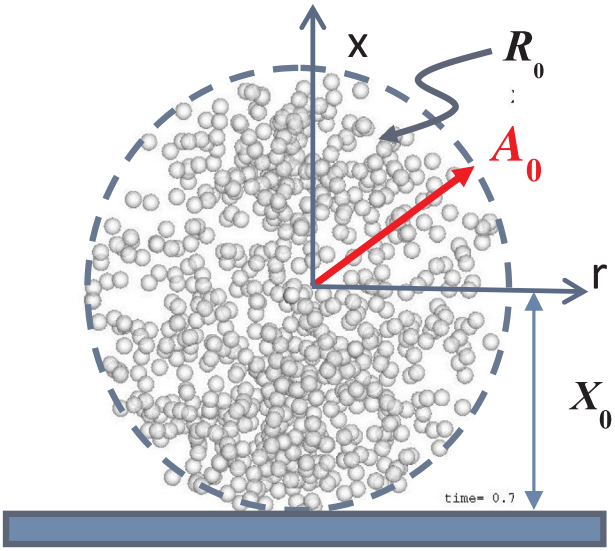

Fig. 3. Schematic of the problem of the dynamics of a bubble cloud near a rigid wall.

3. Results

Fig. 3 shows a cloud of bubbles with an initial overall spherical shape with radius, A_0. The cloud has its center initially at a distance X_0 from the wall, and is composed of small bubbles having the same initial radius, R_0. This is to simplify the presentation and is not a limitation of the software. This bubble cloud is driven by a pressure wave *P*(t):

$$P(t) = P_0 - P_{amp}\sin(2\pi f t) = P_0[1 - \xi\sin(2\pi f t)], \tag{11}$$

where P_0 is the initial pressure at $t = 0$, P_{amp} is the amplitude of the oscillations, *f* is the frequency, and ξ is the normalized oscillation amplitude, $\xi = P_{amp}/P_0$. We select the bubbles to be randomly distributed in the spherical volume, resulting in a quasi-uniform initial void fraction distribution, α_0, within the cloud. At $t = 0$ all the bubbles are in equilibrium with P_0.

We can identify in this problem two groups of parameters: one for the imposed pressure field (amplitude and frequency of the driving pressure) and one for the bubble cloud characteristics (cloud and bubble sizes, void fraction). These determine the dynamics of the bubble cloud. In the following sections, we will investigate the effect of

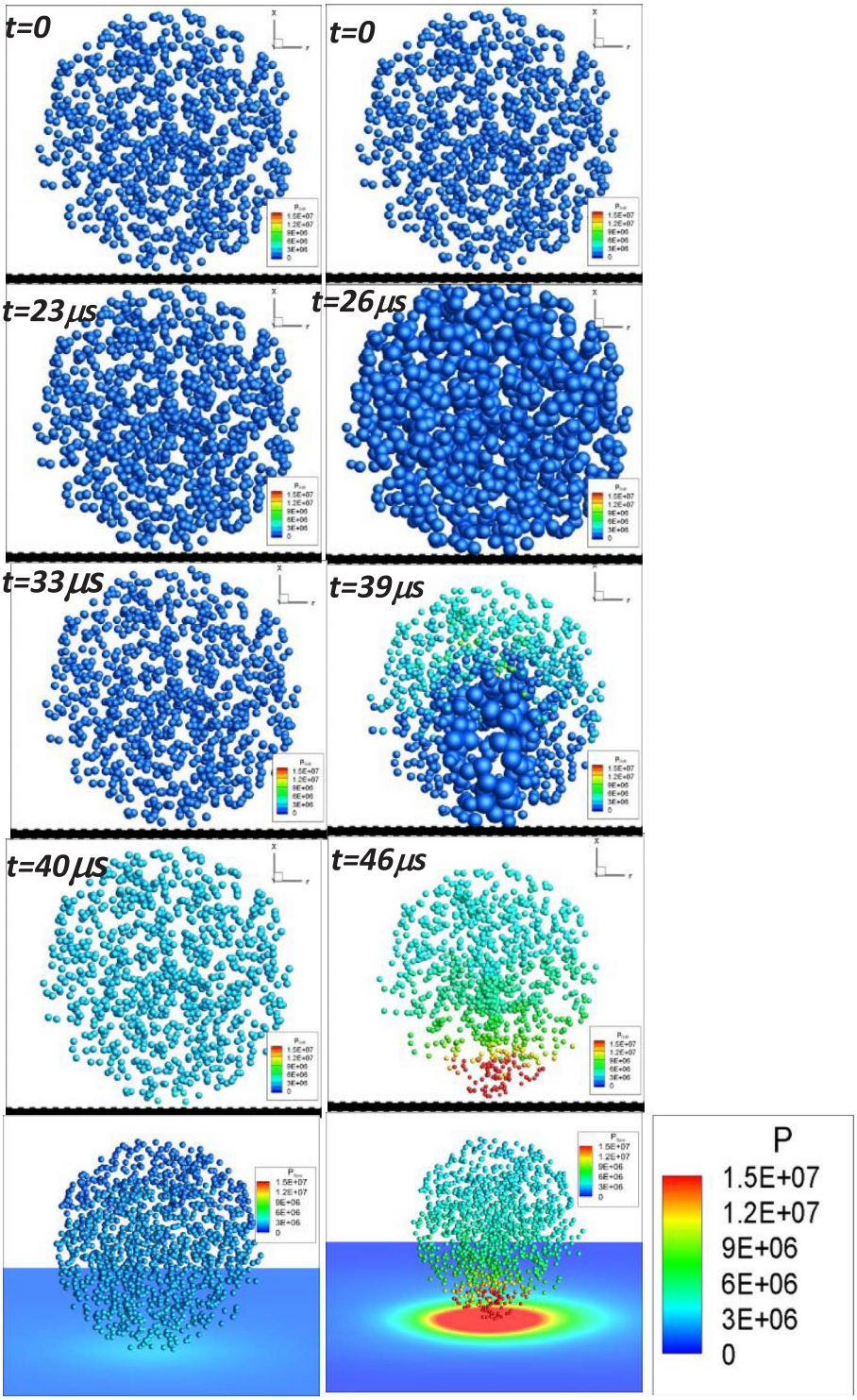

Fig. 4. Time sequence of bubble distributions and internal pressures (indicated by the colored contours) in a bubble cloud driven by pressure excitation with two amplitudes. Left Column: 4 atm ($\xi = 0.4$) and right column: 16 atm ($\xi = 1.6$). For both $P_0 = 10$ atm, $R_0 = 50$ μm, $\alpha_0 = 5\%$, $f = 23$ kHz, and $A_0 = X_0 = 1.5$ mm. The last frame of each row is a view of the pressures at the rigid wall.

these parameters on the bubble cloud dynamics and the resulting pressures at the nearby wall. In this contribution, we do not include bubble breakup or coalescence during the dynamics and these effects, which could be important under certain conditions, are left to future studies.

3.1. Effects of the driving pressure amplitude

The effects of the amplitude of the driving pressure are illustrated in Fig. 4. This figure shows snapshots of the bubble cloud at different instants for $P_{amp} = 4$ atm ($\xi = 0.4$) and $P_{amp} = 16$ atm ($\xi = 1.6$) with the colors indicating the pressure inside each bubble and at the wall (red indicates high inner bubble pressure, i.e. very small bubble, while blue indicates low inner bubble pressure, i.e. very large bubble). The images from top to bottom are for increasing times during the first cycle of the cloud oscillations. In both cases, the bubbles in the cloud grow first then collapse in response to the driving pressure.

Overall, the bubbles in the cloud collapse in a cascading fashion with the bubbles at the cloud top (farthest from the wall) collapsing first and those on the bottom (closest to the wall) collapsing last. As the

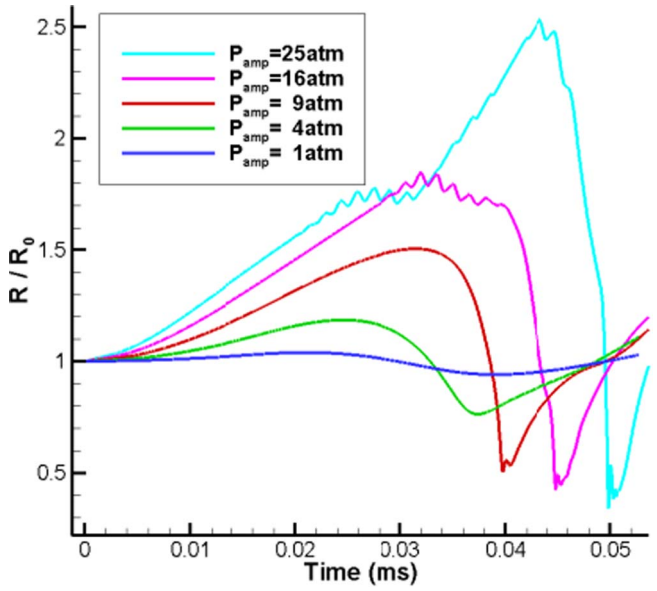

Fig. 5. Size variations of the bubble closest to the wall for different driving pressure amplitudes ($0.1 \leqslant \xi \leqslant 2.5$) for $P_0 = 10$ atm, $R_0 = 50$ μm, $\alpha_0 = 5\%$, $f = 23$ kHz, and $A_0 = X_0 = 1.5$ mm.

amplitude of the driving pressure increases weak bubble oscillations with small amplitudes transform into strong bubble growth and collapse as evidenced by the changes of the bubble sizes visualized by the colors in Fig. 4.

This is made further clear in Fig. 5, which quantitatively compares, the variations of the radius of a bubble close to the wall for increasing relative amplitudes of the pressure, ξ. For $P_{amp} = 1$ atm ($\xi = 0.1$), the radius change is negligible. However, for $P_{amp} = 25$ atm ($\xi = 2.5$), the bubble grows to a maximum radius 2.5 times larger than R_0 and then collapses to a minimum of about 0.3 R_0. Fig. 6 compares the pressure histories monitored at the wall center and shows that the resulting peak increases from 10 atm to about 500 atm for increasing driving pressure amplitudes.

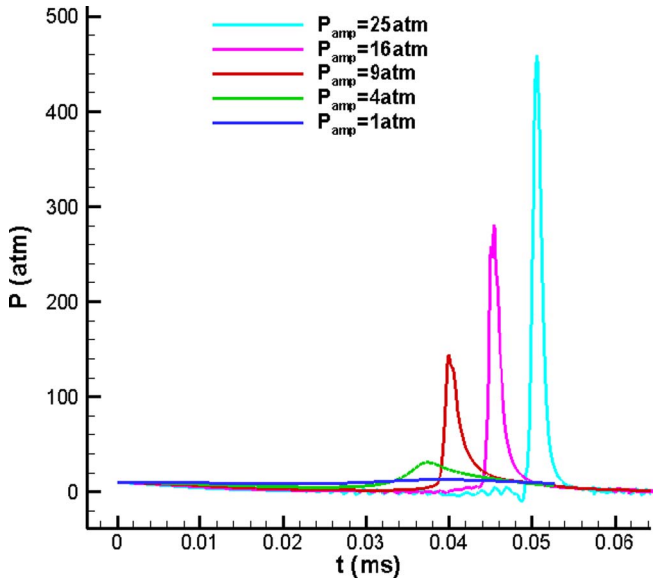

Fig. 6. Pressure at the wall center created by the cloud collapse for different excitation pressure amplitudes ($0.1 \leqslant \xi \leqslant 2.5$) for $P_0 = 10$ atm, $R_0 = 50$ μm, $\alpha_0 = 5\%$, $f = 23$ kHz, and $A_0 = X_0 = 1.5$ mm.

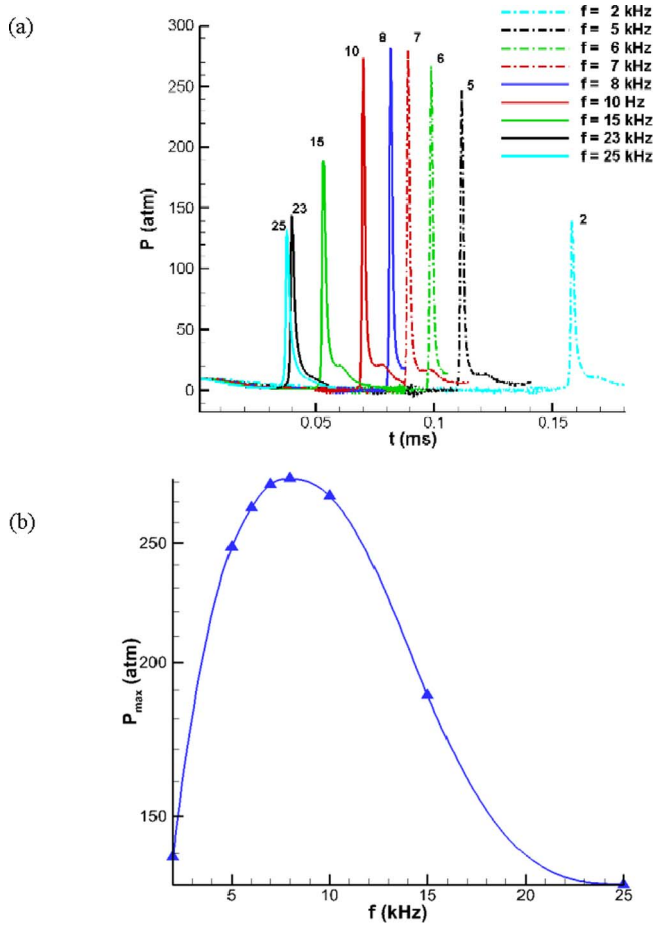

Fig. 7. a) Pressure at the wall center created by a cloud excited at different frequencies. b) Maximum pressure at the wall center as a function of the driving frequency. $P_0 = 10$ atm, $P_{amp} = 9$ atm, $R_0 = 50$ μm, $\alpha_0 = 5\%$, and $A_0 = X_0 = 1.5$ mm.

3.2. Effects of the driving frequency

Tuning between the cloud characteristic frequency and the frequency of the excitation pressure field is essential to generating very high collapse impulsive loads. When the driving pressure frequency matches the characteristic frequency of the bubble cloud, strong collective behavior occurs and very high pressures are generated at the wall. This is illustrated in Fig. 7, which compares for the same pressure amplitude of 9 atm, the effect of the driving frequency on the pressure at the wall. As the figure shows, the cloud behavior is very sensitive to the driving frequency. The highest collective effects here appear to be at 8 kHz and result in a pressure peak of ~300 atm, two orders of magnitudes higher than the excitation pressure.Fig. 8 shows bubble radii versus time for different bubbles in the cloud. Collective behavior (i.e. all bubbles collapse almost simultaneously) occurs when the driving pressure reaches its highest level at the time the individual bubbles start their collapse. This highest pressure forces all bubbles to collapse collectively, i.e. simultaneously. For lower driving frequencies, the pressure reaches its peak too early and drops before the bubbles start their collapse. Conversely, for higher frequencies, the driving pressure reaches its highest value too late and the bubble volumes change is not in phase.

3.3. Resonance frequency of a bubble cloud

It is important to note that the 8 kHz resonance frequency in the cases shown in Fig. 7 and Fig. 8, is much smaller than the reported natural frequency of a cloud, f_{cloud}, derived for small amplitude

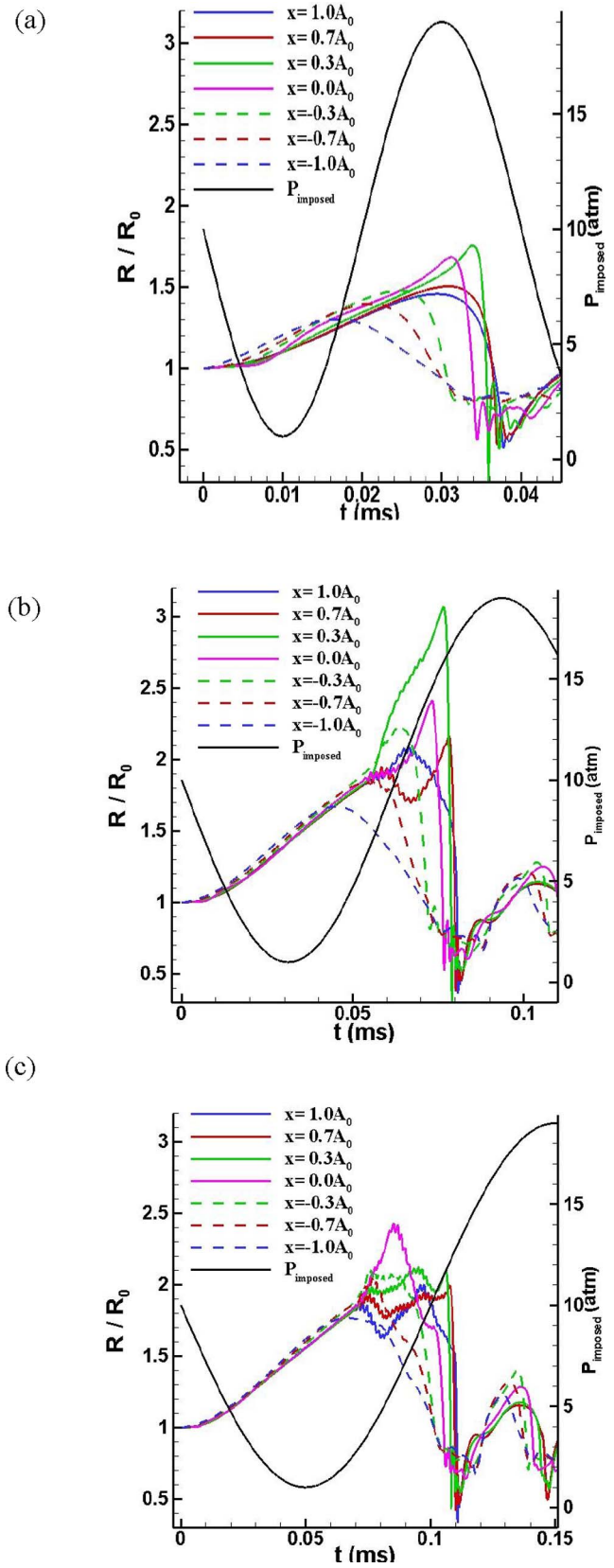

Fig. 8. Comparison of bubble radii at different cloud locations for a bubble cloud excited at different pressure frequencies: (a) f = 25 kHz; (b) f = 8 kHz, and (c) f = 5 kHz for P_0 = 10 atm, P_{amp} = 9 atm, R_0 = 50 μm, α_0 = 5%, and A_0 = X_0 = 1.5 mm.

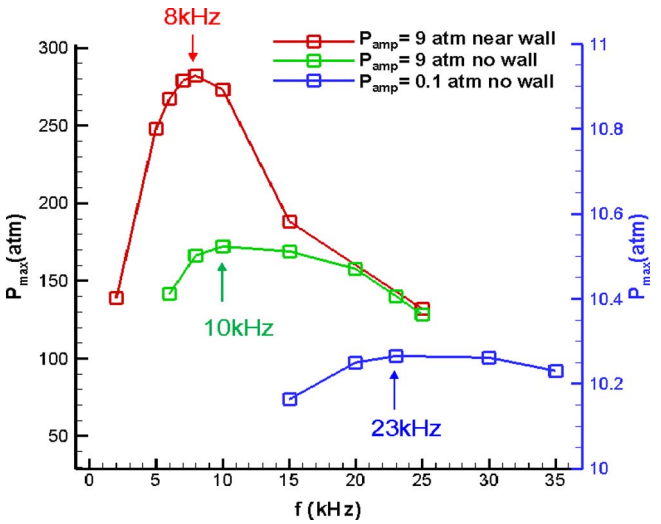

Fig. 9. Comparison of the peak pressures in a range of frequencies obtained for both an isolated bubble cloud and for a bubble cloud near a wall for two driving pressure amplitudes (ξ = 0.01*and*0.9).

oscillations with linear bubble dynamics theory [50]

$$f_{cloud} = f_0\left(1 + \frac{12}{\pi^2}\frac{A_0^2}{R_0^2}\frac{\alpha_0}{1-\alpha_0}\right)^{-1/2} \quad \text{with} \quad f_0 = \frac{1}{2\pi}\sqrt{\frac{P_{g0}}{\rho R_0^2}\left(3-\frac{2\gamma}{P_{g0}R_0}\right)}, \tag{12}$$

which gives a value of f_{cloud} = 23 kHz. Two factors may cause this discrepancy: one is due to the wall proximity effects and the other is due to non-linear effects resulting from high excitation amplitude.

To investigate which factor contributes to the deviation of the resonance frequency from the linear theory prediction, we consider two sets of simulations. The first is conducted with the same driving pressure amplitude, P_{amp} = 9 atm (ξ = 0.9), but in absence of a nearby wall and the second set for a much smaller driving pressure amplitude, P_{amp} = 0.1 atm (ξ = 0.01) again without the nearby wall. The resonance frequency for these two set of simulations can be deduced from Fig. 9, which shows the peak pressure for a range of driving frequencies. It is seen that in absence of the wall, the resonance frequency is only a little higher than 8 kHz, while the resonance frequency matches very well with the linear theory predictions when the driving amplitude is reduced to 0.1 atm (ξ = 0.01). This implies that the driving amplitude is the key factor, which influences the value of the resonance frequency of the bubble cloud.

To investigate further such dependency, Fig. 10 shows the peak pressure as a function of the driving frequency for different values of ξ. From these curves, we can deduce the dependency of the resonance frequency on ξ shown in Fig. 11. It can be seen that when the normalized driving amplitude is less than 0.2, the resonance frequency is well approximated by the linear theory prediction, i.e. 23 kHz. As for nonlinear oscillators, for ξ > 0.2 the resonance frequency deviate significantly from the linear theory results and non-linear interaction effects becomes significant. The value of the resonance frequency decreases almost linearly with increasing ξ until ξ > 1 where the resonance frequency seems to reach a plateau of 5 kHz. A plausible explanation for this saturation is the appearance of inertial cavitation for ξ > 1, where the bubble expansion and collapse are controlled by inertia of the fluid [51].

It is also interesting to consider the dependency on ξ of the peak pressure at resonance frequency. This is illustrated in Fig. 12. It is seen that the peak pressure obtained at the resonance frequency increases from ~10 atm to ~1000 atm as ξ increases from 0.01 to 1.5.

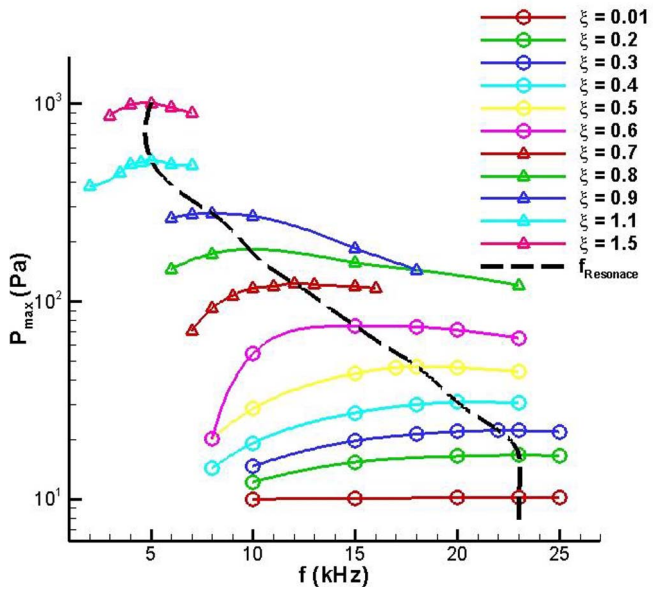

Fig. 10. Peak pressures monitored at the wall center versus driving frequency, for different relative driving pressure amplitudes ($0.01 \leqslant \xi \leqslant 1.5$) for $P_0 = 10$ atm, $R_0 = 50$ μm, $\alpha_0 = 5\%$, and $A_0 = X_0 = 1.5$ mm.

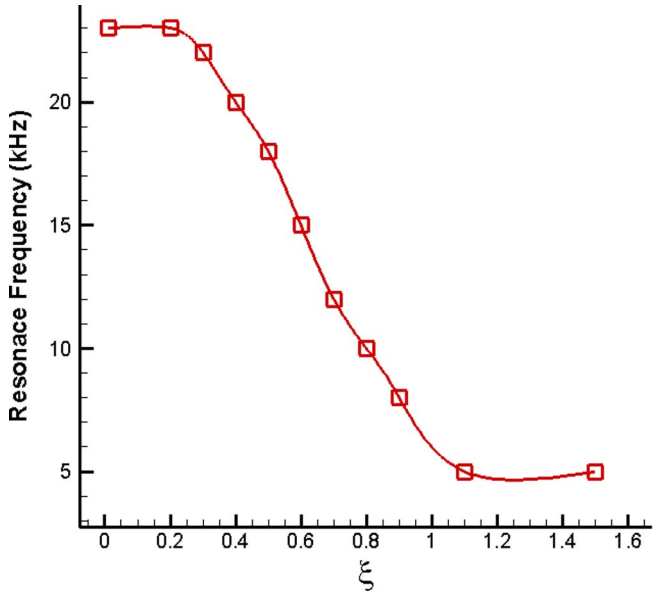

Fig. 11. Bubble cloud resonance frequency versus ξ for $P_0 = 10$ atm, $R_0 = 50$ μm, $\alpha_0 = 5\%$, and $A_0 = X_0 = 1.5$ mm.

3.4. Effects of bubble cloud size on resonance frequency

Eq. (12) implies that the resonance frequency depends also on the initial bubble cloud size, A_0, the initial bubble size, R_0, and the initial void fraction, α_0. In this section, we investigate the dependency of the resonance frequency on the cloud size. Fig. 13 shows the peak pressure as a function of the excitation frequency for different cloud initial radii. As seen in the figure, the peak pressure increases when the cloud overall radius increases while the cloud resonance frequency reduces as the cloud size increases. Fig. 14 examines further the results from Fig. 13 and illustrates that the trend in Eq. (12) is still valid, i.e. the cloud resonance frequency is proportional to the inverse of the normalized cloud size, A_0/R_0 even when non-linear effects are very strong ($\xi = 0.9$). This is made further clear in the right picture of Fig. 14, which presents the same data in a form of $\frac{f_0^2}{f_{cloud}^2} \sim \left(\frac{A_0}{R_0}\right)$. This shows that,

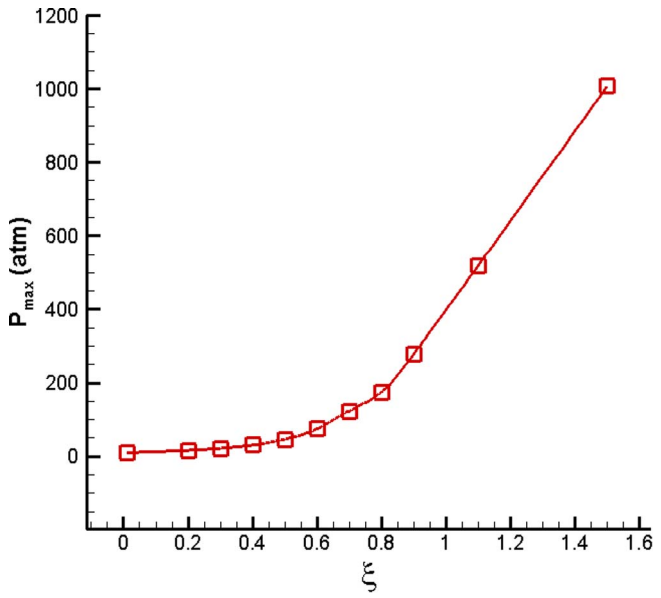

Fig. 12. Peak pressure at the wall versus ξ at bubble cloud resonance frequency for $P_0 = 10$ atm, $R_0 = 50$ μm, $\alpha_0 = 5\%$, and $A_0 = X_0 = 1.5$ mm.

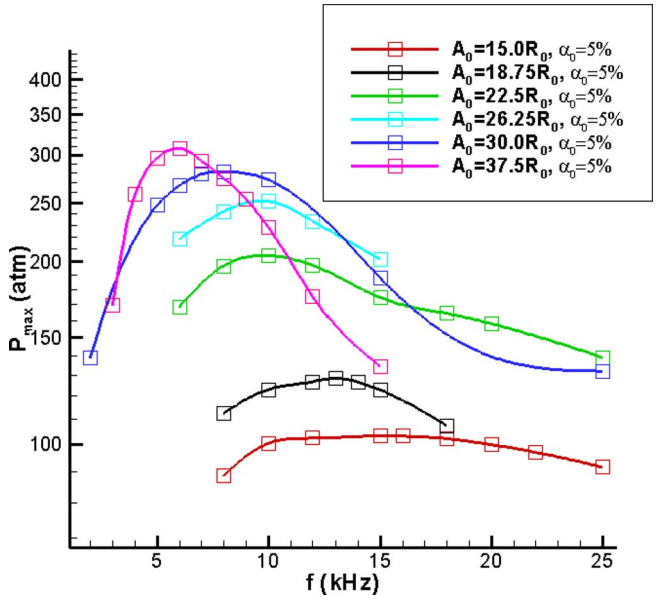

Fig. 13. Peak pressure at the wall center versus driving frequency for different cloud sizes. $P_0 = 10$ atm, $P_{amp} = 9$ atm, $\xi = 0.9$, $R_0 = 50$ μm, $\alpha_0 = 5\%$, and $X_0 = 1.5$ mm.

overall the data falls on a straight line. However, due to strong non-linearities under large amplitude oscillations the slope is much higher than that given by (12)

3.5. Effects of initial void fraction

In this section, we consider the effect of the void fraction on the pressure generated by the bubble cloud dynamics at the nearby wall. In order to do so, we consider a cloud of initial overall cloud radius $A_0 = 1.5$ mm, at an initial standoff distance from the wall, $X_0 = 1.5$ mm, composed of bubbles of initial radii, $R_0 = 50$ μm. In order to change the void fraction, we vary the number of bubbles randomly distributed in the sphere of radius A_0. Fig. 15a shows the pressure versus time for a set of initial void fractions between 1.25% and 15%. All cases are for an initial liquid pressure, $P_0 = 10$ atm and an excitation amplitude, $P_{amp} = 9$ atm ($\xi = 0.9$), and a frequency of

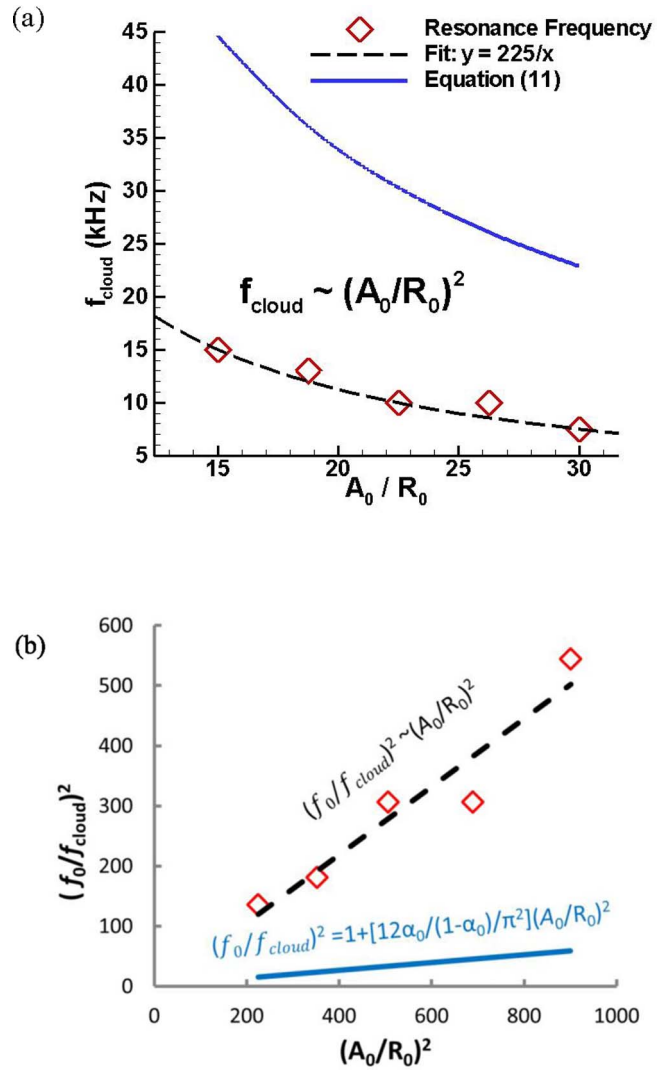

Fig. 14. a) Bubble cloud resonance frequency versus the ratio of initial cloud size to initial bubble size $P_0 = 10$ atm, $P_{amp} = 9$ atm, $\xi = 0.9$, $R_0 = 50$ μm, $\alpha_0 = 5\%$, and $A_0 = X_0 = 1.5$ mm, b) Same data plotted in the form of f_0^2/f_{cloud}^2 versus A_0^2/R_0^2. f_0 and f_{cloud} are the frequencies of a bubble and the cloud, respectively.

f = 8 kHz. The figure shows that the pressure peak at the wall center increases as the initial void fraction increases. However, the rate of increase drops fast to become almost linear as the initial void fraction increases over 3%.

In order to examine whether this increase of pressure is due to the void fraction or to the number of bubbles, Fig.15b shows both P_{max} versus α_0 as well as, an indication of the average contribution of each bubble to the pressure at the wall, P_{max}/N_{bub}, where N_{bub} is the total number of bubbles in each case. The average contribution plot clearly shows that as the initial void fraction increases over 3% the addition of more bubbles (or increase of the initial void fraction) becomes ineffective.

This may be further explained by Fig.15c, which also plots the ratio of maximum void fraction over the initial void fraction as a function of initial void fraction. It is seen that as the initial void fraction increases, the bubbles start interacting in an uncooperative way and prevent each other's growth resulting in a smaller ratio between the maximum bubble cloud gas volume and the initial volume. Best collective effects occur at a small initial void fraction allowing each bubble to grow to each maximum size.

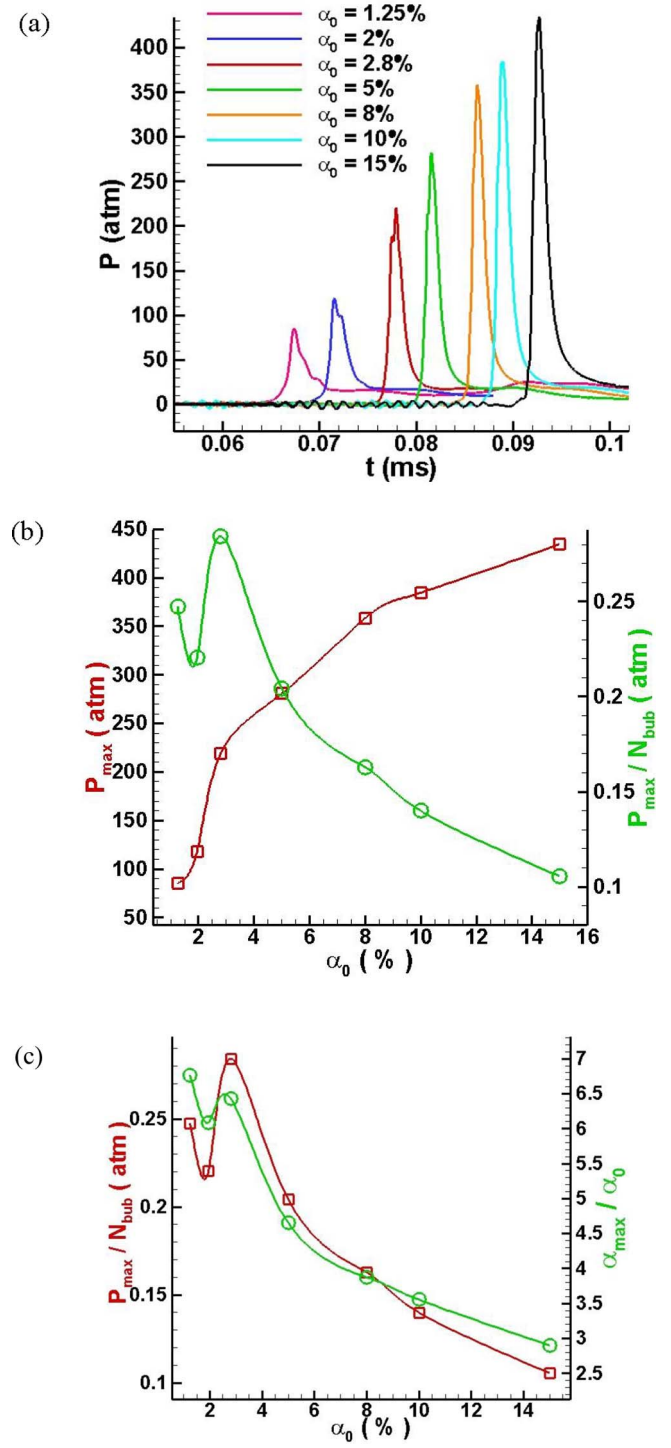

Fig. 15. a) Pressure versus time at the wall center created by bubble clouds with increasing number of bubbles (increasing initial void fraction). b) Maximum pressure at the wall center as a function of the initial void fraction and effective average contribution of each bubble to the pressure at the wall. c) Effective average contribution of each bubble to the pressure at the wall center as a function of the initial void fraction correlated with ratio of maximum void fraction to initial void fraction. For all cases, $P_0 = 10$ atm, $P_{amp} = 9$ atm, $\xi = 0.9$, $R_0 = 50$ μm, $f = 8$ kHz and $A_0 = X_0 = 1.5$ mm.

3.6. Effects of the initial bubble size

In order to investigate, for the same cloud initial void fraction, the effect of the initial bubble radius, we consider a set of cases where we conserve the product $N_{bub}R_0^3$ with N_{bub} is the number of bubbles in the cloud and R_0 is the initial bubble radius. For all cases considered here,

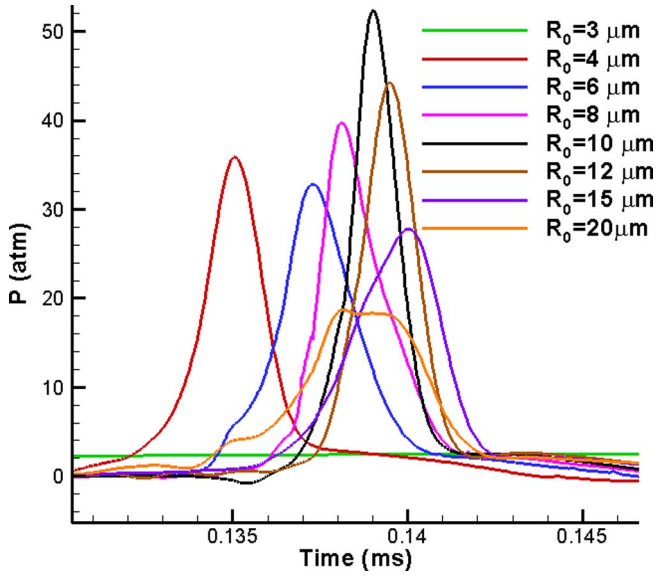

Fig. 16. Peak pressure at the wall center as a function of R_0 for the same initial void fraction in the cloud and $\xi = 1.5$, $P_0 = 1$ atm, $\alpha_0 = 5\%$, $f = 5$ kHz and $A_0 = X_0 = 1.5$ mm.

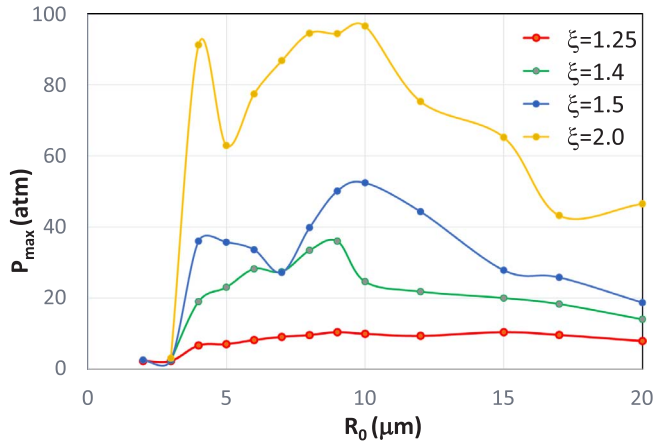

Fig. 17. Peak pressure at the wall center as a function of the initial microbubble size for the same initial void fraction in the cloud. Each curve corresponds to a different relative excitation pressure amplitude ξ. $P_0 = 1$ atm, $\alpha_0 = 5\%$, f = 5 kHz and $A_0 = X_0 = 1.5$ mm.

we conserve all other variables, i.e. overall cloud radius $A_0 = 1.5$ mm, initial liquid pressure, initial void fraction $\alpha_0 = 5\%$, $P_0 = 1$ atm, excitation frequency $f = 5$ kHz, and initial standoff from the wall $X_0 = 1.5$ mm. Note that in this Section, we have elected to look at cases where the ambient pressure is the atmospheric pressure since this is a common condition in ultrasound applications; similar results are obtained for the $P_0 = 10$ atm condition used in the rest of the paper. Fig. 16 and Fig. 17 show the results for R_0 varying between 3 μm and 20 μm (with the corresponding number of bubbles N_{bub} varying between 20640 and 70). Fig. 16 shows, during the first bubble cloud collapse, the time history of the pressure at the wall center for different values of R_0 and for $\xi = 1.5$. It is seen that for the smallest initial bubbles' size, $R_0 = 3$ μm, the pressure sensed at the wall center is practically the same as the driving pressure. The same applies for all radii smaller than 3 μm. This is because, for these small bubble radii, the driving pressure never drops during the oscillations below the bubble critical pressure [52] and the bubbles execute only relatively small amplitude oscillations and never become inertia dominated. This corresponds to the transition referred to as Blake threshold for single bubble dynamics [53].

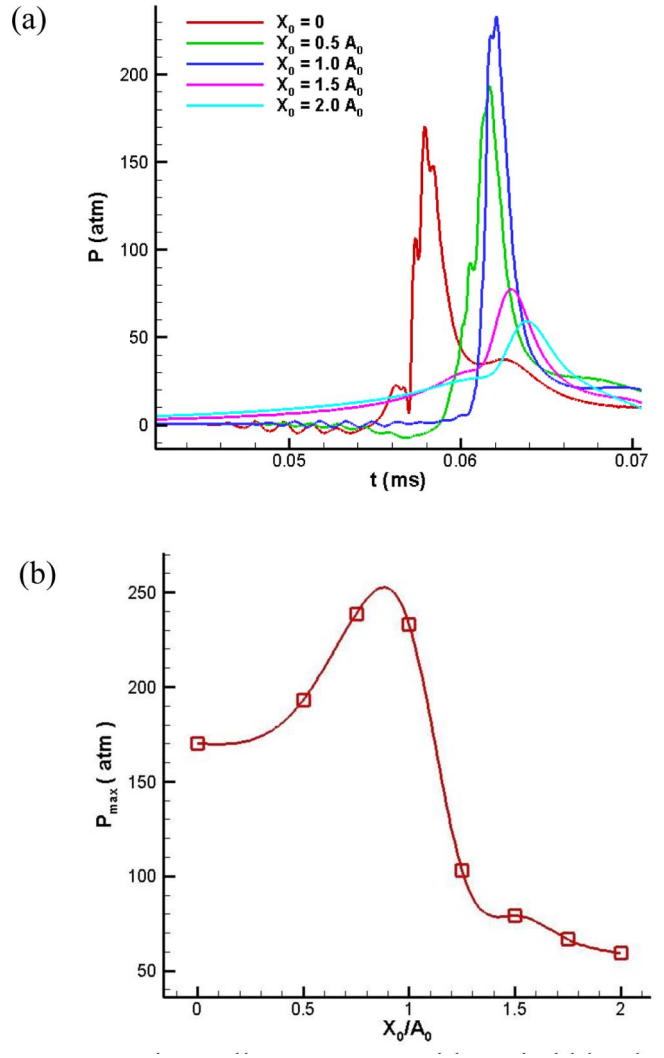

Fig. 18. a) Pressure at the wall center created by a bubble cloud starting at different initial distances to the wall. b) Maximum pressure at the wall center as a function of the initial distances to the wall. $P_0 = 10$ atm, $P_{amp} = 9$ atm, $R_0 = 50$ μm, $f = 12$ kHz and $\alpha_0 = 5\%$.

Right above the threshold a peak pressure is generated, here at 4 μm, as illustrated in Fig. 17 which summarizes the results for four high excitation pressure levels, ξ = 1.25, 1.4, 1.5, and 2.0. For higher values of R_0 another wider peak pressure region is observed between $R_0 = 9$ μm and $R_0 = 10$ μm. This peak requires further investigation and appears to correspond to resonance between the single bubble oscillations and the overall cloud dynamics.

3.7. Effects of initial distance from wall

The effects of the initial distance between the wall and cloud center are studied by varying this distance between two cloud radii and zero. All other parameters are kept the same with $P_0 = 10$ atm, $P_{amp} = 9$ atm, $R_0 = 50$ μm, $A_0 = 1.5$ mm, $\alpha_0 = 5\%$ and $f = 12$ kHz. In order to do so, the bubbles in the portion of the spherical cloud that is located inside the wall are disabled to maintain the value of initial void fraction. The pressure versus time created at the wall center for five standoff distances are compared in Fig. 18. For these conditions, as X_0 increases the peak pressure first increases until reaching its maximum at when the initial standoff is equal to the cloud radius. We can attribute this to the fact that the total number of bubbles is reduced as X_0 decreases and eventually the bubble number is halved when the cloud becomes a half cloud with $X_0 = 0$. In this case, the magnitude of the

peak pressure is only reduced by about half. As X_0 continues to increase beyond the cloud size the maximum pressure generated on the wall starts to decrease. Since whole cloud does not migrate significantly in the vertical direction during the first cycle, the distance between the cloud and the wall at collapse is similar to the initial standoff distance. As a result, the maximum pressure loading simply decreases as X_0 increases.

4. Conclusions

The dynamics of a bubble cloud subjected to a sinusoidal pressure field near a rigid wall is numerically studied. An Eulerian-Lagrangian two-phase flow model is used, where the two-phase medium is modeled using an Eulerian continuum model while the bubbles are considered in a Lagrangian fashion. Simulations involving an initially spherical cloud of bubbles are shown under a range of conditions applicable to cloud cavitation configurations.

Simulations to assess the effect of the amplitude of the driving pressure on the bubble cloud behavior indicate strong nonlinear bubble dynamics effects at large amplitudes. Very strong pressure impact can then be generated at the wall during the cloud collapse. In addition, the resonance frequency of the bubble cloud (i.e. the condition that leads to the strongest bubble collective effect and highest pressures at the wall) is strongly affected by these nonlinear effects. The resonance frequency is found to be much lower than that proposed in the literature using small amplitude oscillations and linearized theory. At high amplitudes of the excitation pressure, the resonance frequency is lower than the linear theory frequency and decreases almost linearly with the ratio of excitation pressure amplitude to ambient pressure.

This resonance frequency is also found to be proportional to the ratio of bubble size to cloud size as in the small oscillations linear theory. The study of initial bubble size effect alone indicates that the maximum peak pressure occurs when the cloud dynamics is such that the maximum bubble radius achieved provides the largest ratio of maximum over initial bubble size.

The initial void fraction is found to have a non-linear effect on the maximum peak pressure when the initial void fraction is smaller than 3%. This effect becomes linear when the initial void fraction is larger than 3%. This indicates that when the void fraction is relatively high, increasing void fraction may cause suppression effects due to bubble-bubble interactions.

The effect of initial distance of bubble cloud from the wall on the bubble cloud dynamics is also studied for several different standoff distances. The maximum peak pressure loading is found when the standoff is of the same order as the cloud radius.

Acknowledgements

This work was supported by the Office of Naval Research under contract N00014-15-C-0052 monitored by Dr. Ki-Han Kim. This support is highly appreciated.

References

[1] L. van Wijngaarden, On the collective collapse of a large number of cavitation bubbles in water, in: 11th Int. Congr. of Appl. Mech, 1964.
[2] L. Wijngaarden, On the equations of motion for mixtures of liquid and gas bubbles, J. Fluid Mech. 33 (3) (1968) 465–474.
[3] L. van Wijngaarden, One-dimensional flow of liquids containing small gas bubbles, Annu. Rev. Fluid Mech. 4 (1972) 369–396.
[4] I. Hansson, V. Kedrinskii, K. Mørch, On the dynamics of cavity clusters, J. Phys. D Appl. Phys. 15 (9) (1982) 1725.
[5] G.L. Chahine, Cloud Cavitation: Theory, in: Proceedings of the 14th Symposium on Naval Hydrodynamics; Ann Arbor Michigan National Academy, 1983, pp. 165–195.
[6] G.L. Chahine, H.L. Liu, A singular perturbation theory of the growth of a bubble cluster in a superheated liquid, J. Fluid Mech. 156 (1985) 257–279.
[7] G.L. Chahine, R. Duraiswami, Dynamical interactions in a multi-bubble cloud, ASME J. Fluids Eng. 114 (4) (1992) 680–686.
[8] J. Ma, C.-T. Hsiao, G.L. Chahine, Euler-lagrange simulations of bubble cloud dynamics near a wall, ASME J. Fluids Eng. 137 (4) (2015) 041301–041310.
[9] M.S. Plesset, A. Prosperetti, Bubble dynamics and cavitation, Ann. Rev. Fluid Mech. 9 (1) (1977) 145–185.
[10] J.R. Blake, D.C. Gibson, Cavitation bubbles near boundaries, Ann. Rev. Fluid Mech. 19 (1) (Jan. 1987) 99–123.
[11] A.J. Coleman, J.E. Saunders, L.A. Crum, M. Dyson, Acoustic cavitation generated by an extracorporeal shockwave lithotripter, Ultrasound Med. Biol. 13 (2) (1987) 69–76.
[12] P. Zhong, Y. Zhou, S. Zhu, Dynamics of bubble oscillation in constrained media and mechanisms of vessel rupture in SWL, Ultrasound Med. Biol. 27 (1) (2001) 119–134.
[13] E.A. Brujan, T. Ikeda, K. Yoshinaka, Y. Matsumoto, The final stage of the collapse of a cloud of bubbles close to a rigid boundary, Ultrason. Sonochem. 18 (1) (2011) 59–64.
[14] D. Krefting, R. Mettin, W. Lauterborn, High-speed observation of acoustic cavitation erosion in multibubble systems, Ultrason. Sonochem. 11 (3–4) (2004) 119–123.
[15] R. Mettin, From a single bubble to bubble structures in acoustic cavitation, Oscil. Waves Interact., 2007, pp. 171–198.
[16] G.L. Chahine, A. Kapahi, J.-K. Choi, C.-T. Hsiao, Modeling of surface cleaning by cavitation bubble dynamics and collapse, Ultrason. Sonochem. 29 (2016) 528–549.
[17] H. Sayyaadi, Enhanced cavitation-oxidation process of Non-VOC aqueous solution using hydrodynamic cavitation reactor, Chem. Engr. J. 272 (2015) 79–91.
[18] G. Loraine, G.L. Chahine, C.-T. Hsiao, P. Aley, Disinfection of gram negative and gram-positive bacterial using dynajets hydrodynamic cavitating jets, Ultrason. Sonochem. 19 (3) (2012) 710–717.
[19] K. Nakashima, Y. Ebi, N. Shibasaki-Kitakawa, H. Soyama, T. Yonemoto, Hydrodynamic cavitation reactor for efficient pretreatment of lignocellulosic biomass, Ind. Eng. Chem. Res. 55 (7) (2016) 1866–1871.
[20] G.L. Chahine, C.-T. Hsiao, R. Raju, Scaling of cavitation bubble cloud dynamics on propellers, Adv. Exp. Numer. Tech. Cavitation Eros. Predict. 160 (2014) 345–373.
[21] K.-H. Kim, G.L. Chahine, J.-P. Franc, A. Karimi, Advanced experimental and numerical techniques for cavitation erosion prediction, Series Fluid Mechanics and Its Applications vol. 106, (2014).
[22] R. Omta, Oscillations of a cloud of bubbles of small and not so small amplitude, J. Acoust. Soc. Am 82 (1987) 1018–1033.
[23] A. Esmaeeli, G. Tryggvason, Direct numerical simulations of bubbly flows Part 1. Low Reynolds number array, J. Fluid Mech. 377 (1998) 313–345.
[24] J. Seo, S.K. Lele, G. Tryggvason, Investigation and modeling of bubble-bubble interaction effect in homogeneous bubbly flows, Phys. Fluids 22 (2010) 063302.
[25] D. Fuster, T. Colonius, Modelling bubble clusters in compressible liquids, J. Fluid Mech. 688 (Oct. 2011) 352–389.
[26] C.T. Crowe, T.R. Troutt, J.N. Chung, Numerical models for two-phase turbulent flows, Ann. Rev. Fluid Mech. 28 (1996) 11–43.
[27] S. Balachandar, J.K. Eaton, Turbulent dispersed multiphase flow, Ann. Rev. Fluid Mech. 42 (1) (2010) 111–133.
[28] R. Raju, S. Singh, C.-T. Hsiao, G. Chahine, Study of pressure wave propagation in a two-phase bubbly mixture, ASME J. Fluids Eng. 133 (12) (2011) 121302–121312.
[29] J. Ma, S. Singh, C.-T. Hsiao, J.-K. Choi, T. Fourmeau, G.L. Chahine, Spherical Bubble Dynamics in a Bubbly Medium, in: International Conference on Numerical Methods in Multiphase Flows, 2012.
[30] C.-T. Hsiao, G.L. Chahine, Effect of a propeller and gas diffusion on bubble nuclei distribution in a liquid, J. Hydrodyn. Ser. B 24 (6) (2012) 809–822.
[31] C.-T. Hsiao, G.L. Chahine, Prediction of vortex cavitation inception using coupled spherical and non-spherical models and Navier-Stokes computations, J. Mar. Sci. Technol. 8 (3) (2004) 99–108.
[32] C.-T. Hsiao, G.L. Chahine, Numerical study of cavitation inception due to vortex/vortex interaction in a ducted propulsor, J. Sh. Res. 52 (2008) 114–123.
[33] X. Wu, J.-K. Choi, C.-T. Hsiao, G.L. Chahine, Bubble Augmented Waterjet Propulsion: Numerical and Experimental Studies, in: 28th Symposium on Naval Hydrodynamics, 2010.
[34] C.-T. Hsiao, X. Wu, J. Ma, G.L. Chahine, Numerical and experimental study of bubble entrainment due to a horizontal plunging jet, Int. Shipbuild. Prog. 60 (1) (2013) 435–469.
[35] J. Ma, G.L. Chahine, C.-T. Hsiao, Spherical bubble dynamics in a bubbly medium using an Euler-Lagrange model, Chem. Eng. Sci. 128 (May 2015) 64–81.
[36] A.J. Chorin, A numerical method for solving incompressible viscous flow problems, J. Comput. Phys. 2 (1967) 12–26.
[37] P.L. Roe, Approximate riemann solvers, parameter vectors, and difference schemes, J. Comput. Phys. 43 (1981) 357–372.
[38] B. van Leer, P.R. Woodward, The MUSCL Code for Compressible Flow: Philosophy and Results, in: TICOM Conference, 1979.
[39] K.J. Vanden, D.L. Whitfield, Direct and iterative algorithms for the three-dimensional Euler equations, AIAA J. 33 (5) (1995) 851–858.
[40] C.-T. Hsiao, G.L. Chahine, H. Liu, Scaling effects on prediction of cavitation inception in a line vortex flow, ASME J. Fluids Eng. 125 (1) (2003) 53–60.
[41] C.-T. Hsiao, G.L. Chahine, Prediction of tip vortex cavitation inception using coupled spherical and nonspherical bubble models and Navier-Stokes computations, J. Mar. Sci. Technol. 8 (3) (2004) 99–108.
[42] J.B. Keller, M. Miksis, Bubble oscillations of large amplitude, J. Acoust. Soc. Am. 68 (2) (1980) 628–633.
[43] A. Prosperetti, A. Lezzi, Bubble dynamics in a compressible liquid. Part 1. First-order theory, J. Fluid Mech. 168 (1) (1986) 457.
[44] C.E.E. Brennen, Cavitation and Bubble Dynamics, Oxford University Press, New York, 1995 vol. 9, no. 1.
[45] W.L. Haberman, R.K. Morton, An Experimental Investigation of the Drag and Shape of Air Bubble Rising in Various Liquids, DTMB Report 802, Sep. 1953.

[46] P.G. Saffman, The lift on a small sphere in a slow shear flow, J. Fluid Mech. 22 (02) (1965) 385–400.
[47] L.A. Crum, Bjerknes forces on bubbles in a stationary sound field, J. Acoust. Soc. Am. 57 (6) (1975) 1363.
[48] A.A. Doinikov, Translational motion of two interacting bubbles in a strong acoustic field, Phys. Rev. E. Stat. Nonlinear Soft Matter Phys. 64 (2) (2001) 026301 Pt 2.
[49] A.A. Doinikov, Bjerkness forces and translational bubble dynamics, vol. 661, no. 2, 2005.
[50] L. D'Agostino, C.E. Brennen, Linearized dynamics of spherical bubble clouds, J. Fluids Mech. 199 (1989) 155–176.
[51] T.J. Matula, Inertial cavitation and single-bubble sonoluminescence, Philos. Trans. R. Soc. A Math. Phys Eng. Sci. 357 (1751) (1999) 225–249.
[52] G.L. Chahine, Y. Shen, Bubble dynamics and cavitation inception in cavitation susceptibility meters, ASME J. Fluids Eng. 108 (4) (1986) 444–453.
[53] I. Akhatov, N. Gumerov, C.D. Ohl, U. Parlitz, W. Lauterborn, The role of surface tension in stable single bubble sonoluminescence, Phys. Rev. Lett. 78 (2) (1997) 227–230.